 doi:10.20944/preprints202103.0177.v1

Article

Warm Advection Fog over the Eastern Yellow Sea: WRF Simulation and Its Verification by Satellite and In Situ Observations

Eunjeong Lee [1], Jung-Hoon Kim [2,*], Ki-Young Heo [3] and Yang-Ki Cho [2]

[1] Korea Institute of Atmospheric Prediction Systems, South Korea, Seoul, South Korea; ejlee@kiaps.org
[2] School of Earth and Environmental Sciences, Seoul National University, Seoul, South Korea; jhkim99@snu.ac.kr; choyk@snu.ac.kr
[3] Korea Institute of Ocean Science and Technology, Busan, South Korea; kyheo21@kiost.ac.kr
* Correspondence: Prof. Dr. jhkim99@snu.ac.kr; Tel.: +82-2-880-6718

Abstract: Sea fog event over the Eastern Yellow Sea on 15–16 April 2012 was reproduced in the Weather Research and Forecasting (WRF) simulation with high-resolution to investigate the roles of physical processes and synoptic-scale flows on advection fog with sea surface warming. Initially, longwave radiative cooling (LRC) with negative sensible heat flux (SHF) due to the turbulence after sunset triggered a formation of cloud at the surface under the moist advection with a southerly wind. This is a conventional type of advection fog. At night, continuous cooling due to longwave radiation and SHF near the surface modulated the change of the SHF from negative to positive, resulting in a drastic increase in the latent heat flux (LHF) that provided sufficient moisture at lower atmosphere (self-moistening). This is a favorable condition for advection fog with sea surface heating (ssH), and this transition represents advection fog with ssH. Enhanced turbulent mixing driven by a buoyancy force increased the depth of the sea fog with a gradual rise in the marine atmospheric boundary layer (MABL) height, even at nighttime. In addition, cold advection with a prevailing northerly wind at the top of the MABL led to a drastic increase in turbulent mixing and the MABL height, which resulted in rapid growth of the height of sea fog due to vertical diffusion. After sunrise, shortwave radiative warming in the fog layers offsetting the LRC near the surface weakened thermal instability, which contributed to the reduction in the MABL height, even during the daytime. In addition, dry advection of northerly wind induced dissipation of the fog via evaporation. An additional sensitivity test of sea surface salinity showed weaker and shallower sea fog than the control due to the decrease in both the LHF and local self-moistening.

Keywords: Advection sea fog; sea surface warming; formation; evolution; dissipation; turbulence

1. Introduction

Fog is defined as cloud reaching to the surface. In particular, fog formed over the ocean, called sea fog, is denser and formed in large areas due to high relative humidity (RH) mainly caused by the ocean. Thus, it moves and dissipates slowly according to the wind. Analysis of sea fog events is important to provide safe and efficient operations in aviation, marine, and road transportation. In addition, these events have an impact on trapping atmospheric pollutant by forming a low capping inversion [1]. Sea fog is generally classified as advection fog or steam fog [2]. Advection fog is formed when air flow passing over a relatively cold or warm ocean is saturated, and is dominant (more than 80% of total sea fog) in the Yellow Sea [3]. It includes warm-sea fog and cold-sea fog phases, depending on the difference in temperatures between the ocean (sea surface temperature; SST) and the atmosphere (surface air temperature; SAT), with a sufficiently moist advection [3–4]. It is defined as advection fog with sea surface heating (ssH) and cooling (ssC) [3], in other words warm and cold advection fogs, respectively. Advection fog with ssH is frequent in spring, but that with ssC is dominant in summer because the SST is generally cooler than the air temperature [5–6]. Steam fog is formed when the water

vapor supplied by surface moisture flux from a relatively warm ocean encounters cold and dry air that leads to subsequent condensation. It frequently forms during winter time over the Yellow Sea or over the Arctic ocean regions due to the fact that the ocean is considerably warmer (typically more than 10 degrees Celsius; evaporative fog) than the atmosphere, which is confined by strong inversion at the top [3,5,7]. Due to the formation of a significantly warmer ocean, steam fog events are less frequent than advection fog events. All of these fogs are dissipated by an increase in atmospheric instability due to warming of the lower atmosphere by sunrise and/or a strong wind shear.

The Yellow Sea between China and the Korean peninsula is a region in which sea fog frequently occurs. It is understood that advection fog with ssH and ssC events is generally frequent in spring and summer, respectively, over the Yellow Sea of the Korean peninsula [3–6]. Accurate prediction of the formation, evolution, and dissipation of sea fog is highly challenging because the difference between SST and SAT is dynamic due to variations in synoptic conditions and ocean currents. Some studies have also emphasized that sea fog is influenced by the synoptic conditions, in addition to local meteorological conditions near the surface [8]. The mechanism of fog with ssC has been studied extensively, and recently more efforts have focused on fog with ssH, which accounts for more than 30% of total advection fog in the western Yellow Sea [3]. Previous research found that, in the transition from ssC to ssH, longwave radiation cooling (LRC) at the top of the surface fog layer plays an important role, and synoptic-scale subsidence pushes down the marine atmospheric boundary layer (MABL) [3]. For the eastern Yellow Sea, clearer understanding is required for the formation, evolution, and dissipation of advection fog events with the transition of the difference between SST and SAT (SST-SAT), in accordance with the MABL and underlying background conditions. In particular, the synoptic conditions near the Korean peninsula in spring can change immediately between cold/dry and warm/moist air flows, which results in the occurrence of advection fog with ssH. To fully understand advection fog with ssH in different areas, additional case studies of multiple vertical layers in the MABL are required.

Numerous attempts have been made to study the detection or mechanism of sea fogs using both observations and numerical simulations. For example, an algorithm for a warm fog detection using a combination of Geostationary Operational Environmental Satellite-12 (GOES-12) observations and screen temperature data based on a Canadian operational numerical model was developed [9]. They suggested that the detection of the warm fog from the satellite-based algorithms can be improved by including model-based sounding values. A parameterization scheme for warm-fog visibility was introduced using in-situ observations and combined parameters such as droplet number concentration and liquid water content from a numerical weather prediction model [10]. Besides, it was found that the uncertainty of Arctic clouds decreased by considering the origin of the air mass obtained from the numerical model [11]. All these previous studies suggested that numerical models are important factors for accurate detection of fog or low-level clouds [10]. Meanwhile, a simulation of fog with ssC was investigated using numerical prediction models and was compared with satellite data [12]. The authors reported that the top height of sea fogs estimated from the observation was observed to be less than 500 m. However, those estimated using a simulation from the Weather Research and Forecasting (WRF) model tend to be overestimated, showing the top of the fogs to be greater than 1500 m height, and coupling with a one-dimensional turbulence model is likely to suppress the overestimation. They also mentioned that sea fog is formed by the turbulent exchange of heat and moisture, the diurnal variation in radiation, and advected air flows over the sea surface, and that turbulent heat and moisture fluxes modify the environment of temperature and humidity within the MABL. In addition, the ascent of the fog top may be related to the turbulence that enhances the entrainment mixing of the relatively humid air from above the fog top. It is expected that the turbulence in the MABL, which has a close interaction with radiation and advection processes, plays an important role during the duration of

 doi:10.20944/preprints202103.0177.v1

the formation and dissipation of the sea fog. Unlike studies of the formation mechanism of sea fog, few studies have focused on the dissipation mechanism of sea fog.

This study aimed to understand the mechanisms of formation, evolution, and dissipation of advection fog with ssH over the eastern Yellow Sea using high-resolution numerical simulation. In particular, this study attempted to understand five factors: 1) the impact of the change in temperature and moisture due to turbulent fluxes, radiative fluxes, and thermal and moisture advection on the formation and dissipation of sea fog; 2) the role of the change in synoptic-scale flows (e.g., transition from warm/moist advection to cold/dry advection) in the growth of the MABL; 3) the influence of the resulting MABL evolution on the vertical diffusion of fog due to turbulence intensified by mechanical and buoyant forcing; 4) the dependency of the mechanisms of sea fog on the regions; and 5) the impact of sea surface salinity on simulated sea fog. For this purpose, we investigated the mechanisms of sea fog with their related physical processes, focusing on the interactions between the surface turbulent flux, MABL height, and tendencies of temperature, water vapor (Qv), and cloud liquid water content (Qc), using a numerical simulation of sea fog during the spring season. This paper is organized as follows: Section 2 describes the model and experimental design. Synoptic-scale flows and spatial distributions of sea fog from satellite and sounding observations, and a WRF simulation, and a brief description of the selected events, are examined in Section 3.1 to examine the performance of the model for advection fog with ssH. Relevant physical processes, in particular the process associated with turbulence, in terms of the formation, evolution, and dissipation, are discussed in Section 3.2. In addition, a sensitivity test of salinity effect is also examined in this section. Finally, conclusions are outlined in Section 4.

2. Model and experimental design

The WRF model version 4.0 was used for the sea fog case simulation [13]. This study focused on a sea fog event over the eastern Yellow Sea. The experiment has four nested domains, including the East Asian region centered over the eastern Yellow Sea of the Korean Peninsula, with horizontal resolutions of 27, 9, 3, and 1 km (Fig. 1). It employs 51 vertical eta levels with a model top of 50 hPa, of which 15 layers are located at the lower atmosphere below about 950 hPa because the sea fog event usually occurs near the surface. Physical schemes employed in this study included the Yonsei University (YSU) boundary layer scheme [14], the WRF double-moment 6-class microphysics scheme (WDM6) [15], the Rapid Radiative Transfer Model (RRTM) for the radiation scheme [16], the unified Noah land surface model [17–19], and the revised MM5 Monin–Obukhov surface layer scheme [20]. The Kain–Fritsch cumulus parameterization scheme [21] was used only for domains 1 and 2.

Preprints (www.preprints.org) | NOT PEER-REVIEWED | Posted: 5 March 2021 doi:10.20944/preprints202103.0177.v1

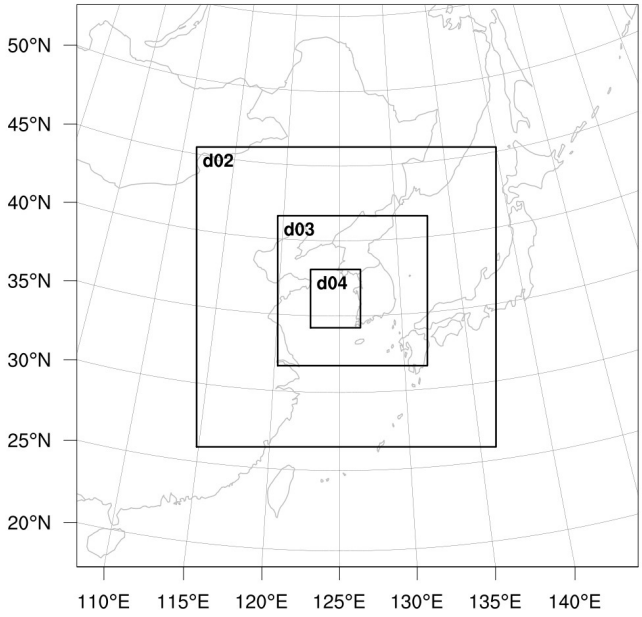

Figure 1. Geographical map of the eastern Yellow Sea and its neighboring regions with four model domains.

A sea fog event observed by satellite data over the Yellow Sea of the Korean peninsula on 15–16 April, 2012 was selected in this study. The simulation was carried out for 36 h forecasts initiated at 0000 UTC 15 April 2012. The initial atmospheric and bottom boundary conditions were taken from the National Centers for Environmental Prediction (NCEP) Global Forecast System Final Analysis (GFS-FNL) dataset with 1° × 1° spatial resolution, and the optimal interpolation sea surface temperature (OISST) with 0.25° × 0.25° spatial resolution, respectively. For boundary conditions in the child domains, one-way nesting domains were used. Details for the experimental setting of the WRF model and the configuration of the physics package are given in Tables 1 and 2, respectively.

Table 1. Experimental settings of the Weather Research and Forecasting (WRF) model.

Model	WRF v4.2
Nesting method.	One-way data
Horizontal resolution	4 domains (27, 9, 3, 1 km)
Vertical levels (eta levels)	51 levels
Time step (s)	180 s (D1), 60 s (D2), 20 s (D3), 6.6 s (D4)
Initial and Boundary Conditions	Atmos: NCEP FNL (1° × 1°), SST: daily OISST (0.25° × 0.25°)

Table 2. Configuration of the physics package.

Process	Scheme
Radiation	RRTM (SW), Duhia (LW)
Microphysics	WRF Double-Moment 6-class (WDM6)
Deep cumulus	Kain–Fritsch cumulus parameterization scheme
Planetary boundary layer	Yonsei University (YSU)
Land surface	Unified Noah land surface model
Surface layer	Revised MM5 Monin–Obukhov surface layer scheme

 doi:10.20944/preprints202103.0177.v1

3. Results

3.1. Case overview

3.1.1. Synoptic-scale flows

Figure 2 shows the horizontal distributions of mean sea level pressure with a 10 m wind at 1200 UTC (2100 KST) and 0000 UTC (0900 KST) on 15 April 2012, and 1200 UTC on 16 April 2012, obtained from the Korea Meteorological Administration (KMA) and simulated by the WRF model. On 15 April 2012, a local high-pressure system, which originated from the Siberian high-pressure system centered at central China, was separately located in the south-western region of the Yellow Sea of the Korean peninsula, and a weak low-pressure system was located in Wonsan bay in eastern Korea. Thus, it could be expected that the west coast of Korea was affected by a weak south-westerly wind with a weak pressure gradient. It was found that the northern parts of the Yellow Sea were affected by warm and moist air flows under this synoptic condition (Fig. 2a). Then, the synoptic-scale fields changed at 0000 UTC 16 April because the continental high-pressure system in north China quickly expanded to the northern Yellow Sea. This led to a high-pressure system to the north of Korea and a low-pressure system to the south of Korea at this time (Fig. 2c). Therefore, it induced a cold and dry air flow due to the presence of northerly winds. The synoptic-scale conditions with northern winds were maintained until 1200 15 April 2012 (Fig. 2e).

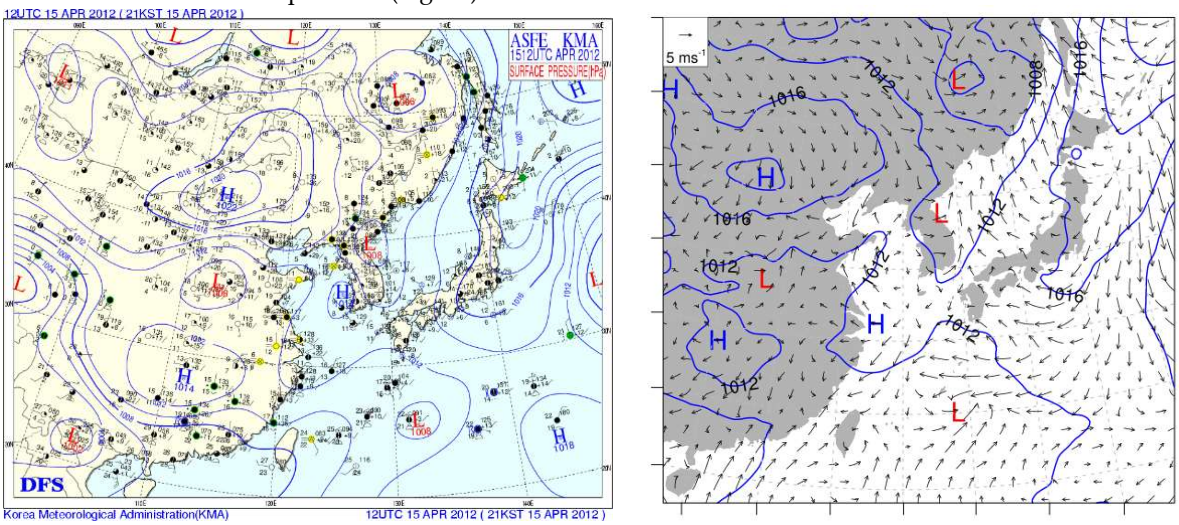

(a) **(b)**

Preprints (www.preprints.org) | NOT PEER-REVIEWED | Posted: 5 March 2021 doi:10.20944/preprints202103.0177.v1

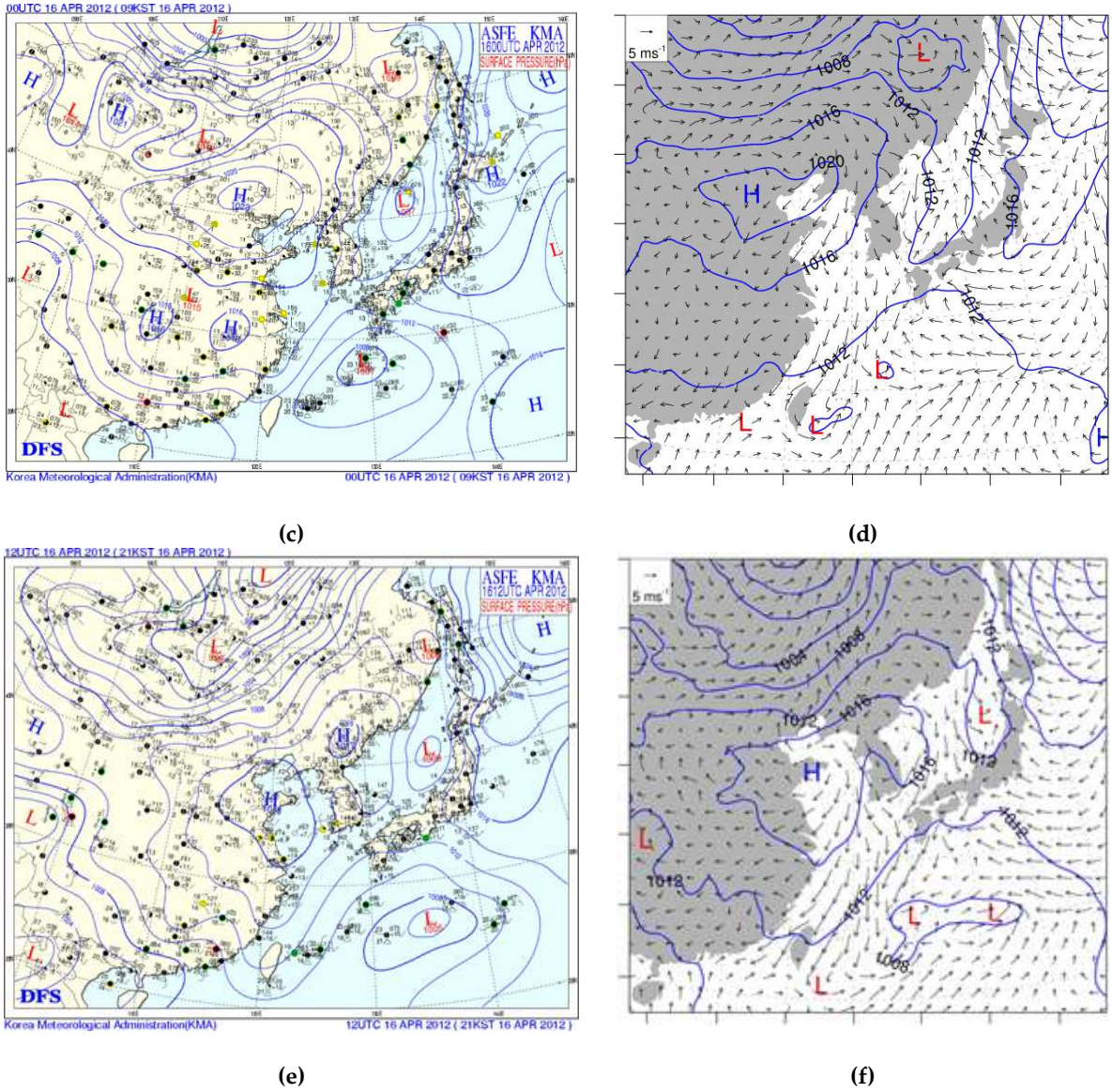

Figure 2. Synoptic weather charts for sea level pressure (SLP) (a, c, and e) generated by the Korea Meteorological Administration (KMA), and (b, d, and f) simulated for domain 1; (a and b) 1200 UTC on 15 April 2012, (c and d) 0000 UTC on 16 April in 2012, and (e and f) 1200 UTC on 16 April in 2012. Wet areas shaded with green dots are defined as T-Td < 3 K and the arrows indicates a 10 m wind (m s^{-1}).

In the spatial patterns of the simulated mean sea level pressure shown in Figures 2b, 2d, and 2f, it can be seen that synoptic-scale conditions shown in the analytical surface weather chart were reproduced correctly in the simulation. In detail, the high-pressure system to the west of the Korean peninsula and the low-pressure system to the east of the Korean peninsula, and the south-westerly wind, are consistent with the simulated result at 1200 UTC on 15 April 2012. Then, at 0000 UTC on April 16, the continental high-pressure system centered at north China expanded to the western region of Korea, and the low-pressure system was located in the southern part of the Korean peninsula. Subsequently, the western part of the Korean peninsula was dominated by the anticyclonic flow due to the movement of the high-pressure system. Overall, it was expected that the synoptic-scale conditions at 1200 UTC on 15 April 2012 and 0000 UTC 16 April 2012, in both analytical and simulated surface weather charts, supported the fine weather condition during this period. This case had good synoptic-scale conditions with a change from a

Preprints (www.preprints.org) | NOT PEER-REVIEWED | Posted: 5 March 2021 doi:10.20944/preprints202103.0177.v1

warm/moist air flow to a cold/dry air flow for the formation of both fog with ssC and fog with ssH, in which the air–sea interaction meets the formation of the cloud near the surface. Eventually, the transition of the sea fog from ssC to ssH could occur under this condition. The distribution of the sea fog observed by satellite data is presented in the next section.

3.1.2. Distribution and verification of sea fog

To verify sea fog simulated from the WRF model, the spatial distribution of sea fog from the observed data and simulation were compared. Figures 3a, 3c, and 3e depict near-infrared images obtained from the Communication, Ocean and Meteorological Satellite (COMS) operated by the National Meteorological Satellite Center of Korea (https://nmsc.kma.go.kr/homepage/html/main/main.do) at 1200 UTC on 15 April 2012, and 0000 UTC and 1200 UTC on 16 April 2012, which can detect the spatial distribution of fog, expressed with an orange color. It was shown that sea fog began to form over the northern part of the Yellow Sea after sunset at 1200 UTC 15 April 2012 (Fig. 3a). Then, the fog gradually developed at night, with an extension to the southeast; consequently, it covered the entire part of the Yellow Sea between China and Korea at 0000 UTC 16 April (Fig. 3c). This image shows that the event is a suitable case to investigate the sea fog because cumulus or cirrus clouds on top of the fog layer were not observed when there was a large fog patch over the Yellow Sea. The fog was almost dissipated in most regions, leaving only a small portion in the south of the Yellow Sea at 1200 UTC 16 April 2012 (Fig. 3e). Regarding the presence of sea fog, it was also confirmed in the surface weather chart (Figs. 2a and 2c) that the weather symbol for fog (yellow shading at a designated station model) was reported at Baeknyeong island (the location is depicted as the red cross at "A" in Fig. 3b) at 1200 UTC on 15 April and 0000 UTC on 16 April 2012, while it was also reported at Heuksan Island (the location is depicted as the red cross at "B" in Fig. 3b) at 1200 UTC 16 April 2012 (Figs 2a, c, and 2e). The distribution of the average of the simulated Qc for the levels below z = 500 m for domain 3 is plotted as blue shading in Figures 3b, 3d, and 3f. Sea fog in the simulation was inferred through the areas with an average Qc higher than 0.01 g kg^{-1}. Locations of A and B, marked with red-cross signs in the figures, refer to the stations at Baeknyeong and Heuksan islands, respectively. It can be observed that the spatial distribution of the sea fog was well simulated in the WRF model, although it shows a local discrepancy in slow occurrence or slow movement in some areas.

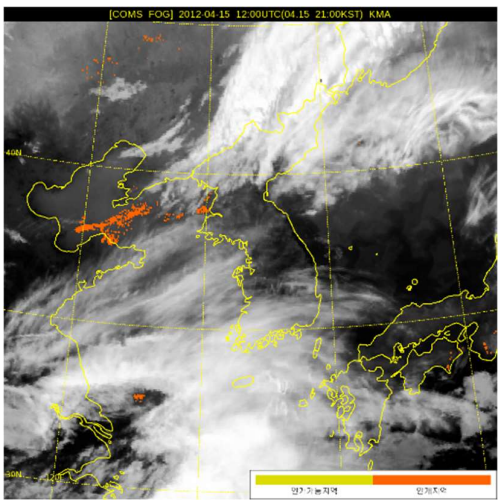

(a)

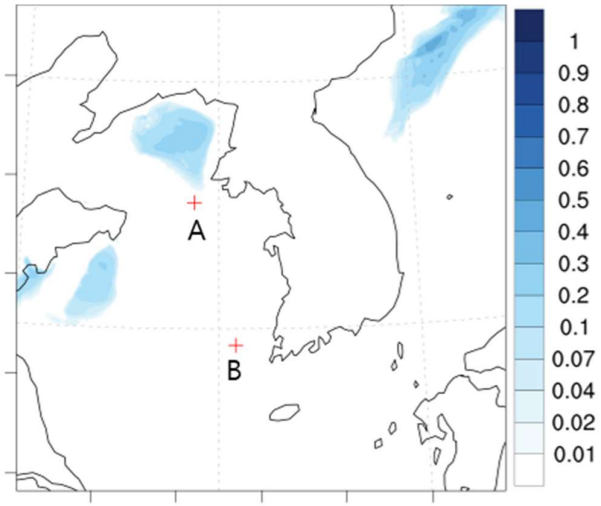

(b)

Preprints (www.preprints.org) | NOT PEER-REVIEWED | Posted: 5 March 2021 doi:10.20944/preprints202103.0177.v1

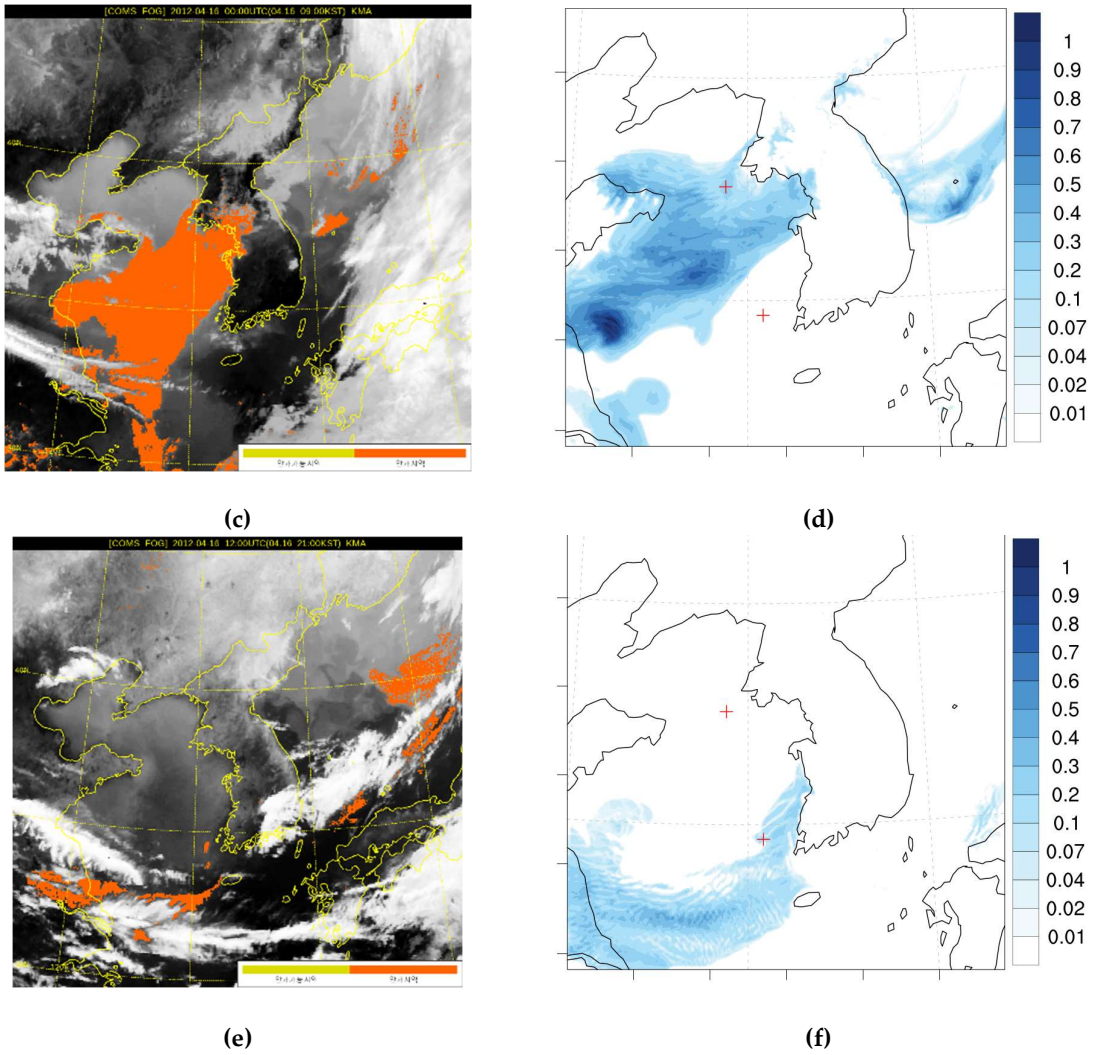

Figure 3. (a, c, e) Near-infrared images from the Communication, Ocean and Meteorological Satellite (COMS) operated by the KMA and (b, d, f) distributions of simulated Qc (g kg^{-1}) averaged for the levels lower than a 500 m height for domain 3; (a, b) 1200 UTC on 15 April, (c, d) 0000 UTC on 16 April, and (e, f) 1200 UTC on 16 April in 2012. Fog areas are denoted by yellow (potential) and orange (detected) shading in the near-infrared images. The cross signs indicate the oceans near Baekneyong island (124.38°E, 37.55°N) and Heuksan island (125.42°E, 34.67°N) stations, respectively, that provide data from sounding observations.

Figure 4 shows the evolution of vertical profiles (time–height cross-sections) of the simulated relative humidity (RH; top panel) and Qc (bottom panel) averaged within the 50 × 50 km areas centered at regions A and B. The simulated MABL height at each region is superimposed in Figs. 4a and b. In region A (Figs. 4a and 4c), formation of the fog begins to form at the near-surface layer at 1200 UTC on 15 April, and the height of the fog gradually increases with time, and then the maximum height of the fog is shown in early morning at around 2200 UTC on 15 April 2012. Finally, it started to dissipate above the MABL. To verify the simulated sea fog, the top heights of the observed sea fog estimated from MeTeorolgical SATelite-2 (MTSAT-2) geostationary satellite data are superimposed in Figures 4c and 4d, following the method mentioned in a previous study [12]. To detect nighttime sea fog, the difference in brightness temperatures between the 3.8 and 10.8 μm channels in the MTSAT-2 satellite data was determined [22–23]. The fog-top height was estimated from the difference between the two channels [24]. Note that satellite-based warm fog detection based on the algorithms using satellite data had an accuracy less than

Preprints (www.preprints.org) | NOT PEER-REVIEWED | Posted: 5 March 2021 doi:10.20944/preprints202103.0177.v1

60% and the algorithms based on only brightness temperature difference between channels could not work accurately when an elevated fog layer occurs [9]. Accordingly, although the sea fog is shown in region A from the MTSAT-2 fog-top results, the presence of sea fog is unclear from 0000 UTC to 0700 UTC 15 April according to the weather charts. Thus, this study focused on the sea fog event over the eastern Yellow Sea during the period from 1000 UTC 15 to 1200 UTC 16 April. Observed sea fog was well simulated in the numerical model experiment during the sea fog event, although overestimation of the top heights was found in the simulation. The formation and dissipation phases of the sea fog estimated from the MTSAT-2 occurred at about 1200 UTC on 15 April 2012 and 0400 UTC on 16 April 2012, respectively. Somewhat earlier formation and delayed dissipation of sea fog was found in the simulation. However, it can be understood that the formation and dissipation timings were predicted well in the numerical model experiments. In region B (Figs. 4b and 4d), unlike in region A, at 04 UTC on 16 April 2012 the sea fog started to form at a height of about z = 200 m with a low RH, whereas that in region A was formed from the surface with a sufficiently high RH. Thus, it can be expected that mechanisms for sea fog depend on the regions. Detail mechanisms are discussed in the next section. Consequently, we can investigate mechanisms for the sea fog from the numerical simulation, because both spatial and temporal distributions of the observed sea fog event are reproduced accurately in the model.

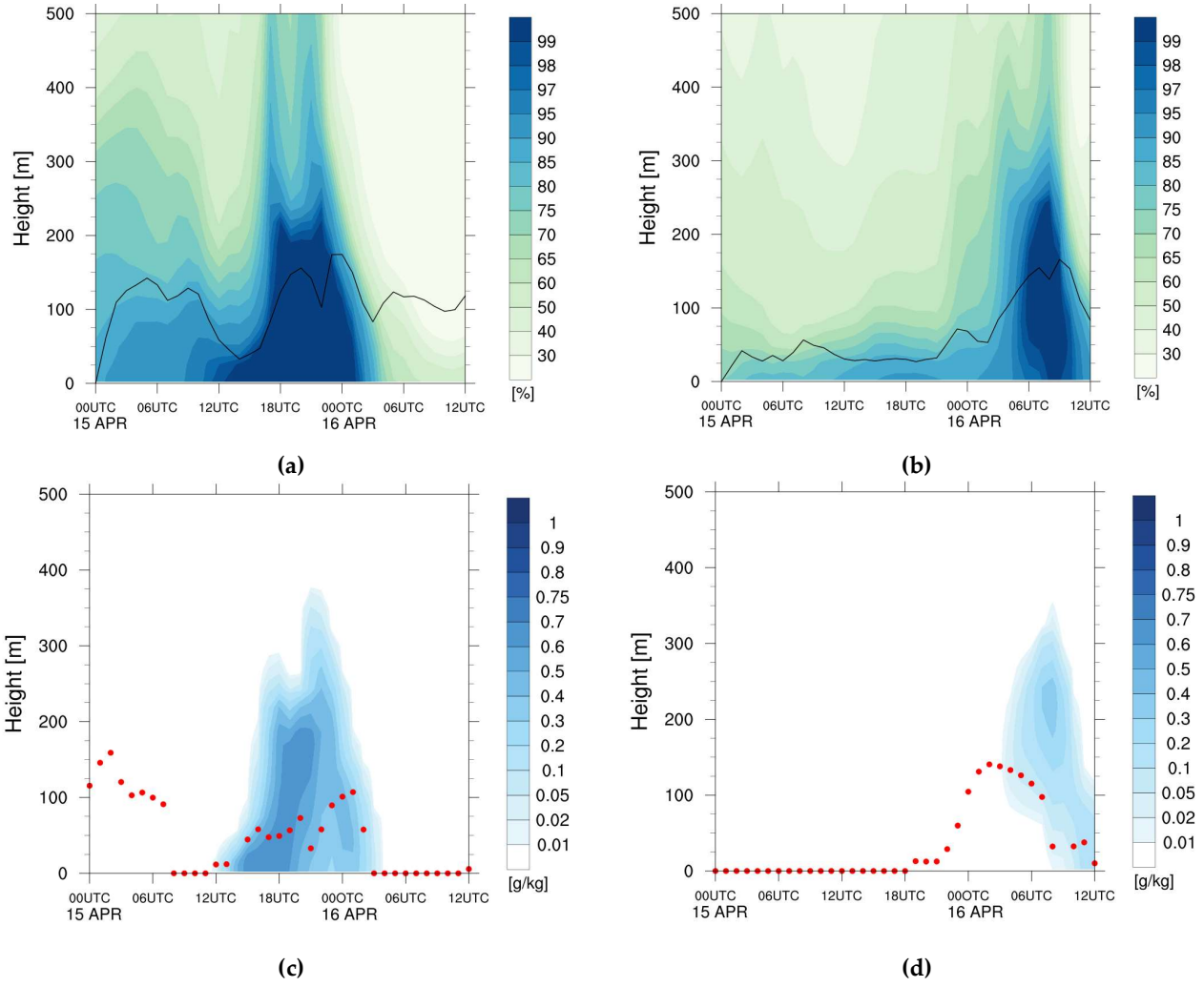

Figure 4. Evolution of vertical profiles of the (a, b) relative humidity (RH; %) with the marine atmospheric boundary layer (MABL) height (thick solid line, m) and (c, d) Qc (g kg^{-1}) with the estimated height of the fog top from the MTSAT-2

 doi:10.20944/preprints202103.0177.v1

satellite data (dot, m) in domain 4, averaged over the nearby oceans; (a, c) Baeknyeong island (hereafter region A) and (b, d) Heuksando island (hereafter region B).

Figure 5 shows the vertical profiles of temperature and humidity simulated in the numerical model with the observed sounding data. In general, the simulated temperature and humidity at the time when the sea fog was dominant at the two stations showed good agreement with the observed data. In particular, at region A (Baeknyeong Island) the temperature profile simulates an inversion layer between 200 and 400 m, and it can be inferred that the condensation layer formed below it (i.e., the fog layer) will be trapped. Although there is a slight difference in the humidity profile, it has the maximum value in the lower layer and gradually decreases from the height at which the inversion layer begins, which is similar to that observed. The fog-top height in the numerical model increased to more than 300 m, whereas those inferred from the sounding data and from the MTSAT-2 were limited to about 200 m during the duration of the fog event. Note that the depth of the sea fog tended to be overestimated in the current numerical simulation, which is somewhat consistent with previous studies [25–28].

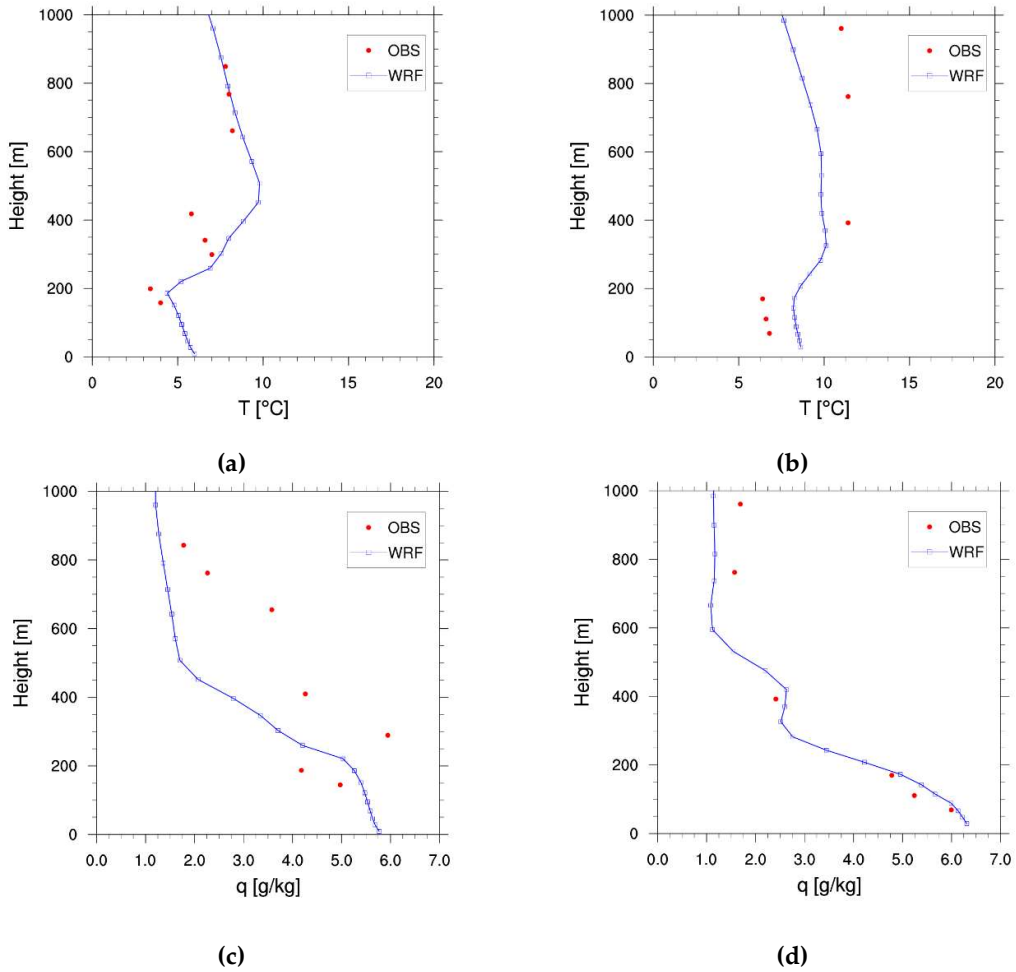

Figure 5. Comparison of observed (red dots) and simulated (blue solid lines) vertical profiles of the (a, b) temperature (°C) and (c, d) specific humidity (g kg^{-1}) during the fog event (a, c) at the Baeknyeong island station at 0000 UTC 16 April 2012 and (b, d) at the Heuksan island station at 1200 UTC 16 April 2012.

Preprints (www.preprints.org) | NOT PEER-REVIEWED | Posted: 5 March 2021 doi:10.20944/preprints202103.0177.v1

3.2. Mechanism of sea fog

To understand the mechanisms of the sea fog, we investigated related physical processes in the stages of formation, growth, vertical jump, and dissipation at each of regions A and B.

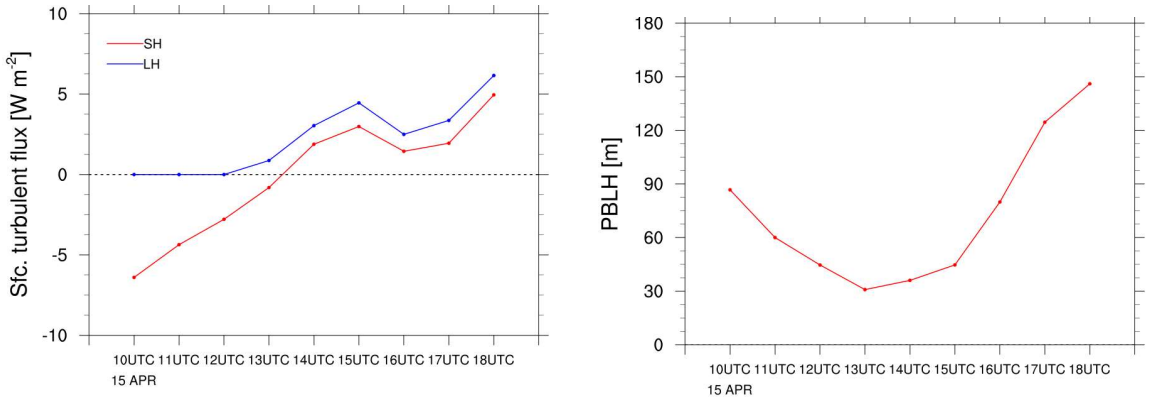

(a) **(b)**

Figure 6. Time series of the (a) surface turbulent fluxes (blue: latent heat flux; LHF, red: sensible heat flux; SHF) and (b) MABL height in region A during the formation and evolution stages.

3.2.1. Formation stage

We first investigated the changes of temperature and hydrometer at the surface and the lowest model level (z_1), because the formation of sea fog in region A started near the surface. The time series of surface turbulent fluxes and the MABL height in region A at the formation and evolution stages are displayed in Figure 6. The positive (negative) turbulent fluxes indicate upward (downward). Time series of hourly accumulated tendencies of the temperature, Qv, and Qc at z_1 in the same region and period are also shown in Figure 7. Before the onset of the formation of sea fog (until 1000 UTC on 15 April 2012), the ocean was colder than the lower atmosphere, and negative sensible heat was caused by the turbulence due to the difference between the SST, SAT, and frictional velocity, resulting in decreases in SAT (Fig. 6a and red line in Fig. 7a). At the same time, the tendencies of temperature and Qv at z_1 indicate that region A was affected by warm and moist advection in line with the southerly wind (green lines in Figs. 7a and 7b). Due to atmospheric cooling and moist advection in the lower atmosphere, RH near the sea surface was sufficiently high (close to 100%) (Fig. 4a). Because shortwave radiative (SW) warming ends after sunset, LRC is dominant (blue line in Fig. 7a). Cooling near the surface due to turbulent and radiative fluxes overwhelmed warming by advection at 1100 UTC on 15 April 2012 (black line in Fig. 7a), and triggered condensation near the surface due to microphysics process at 1200 UTC on 15 April 2012 (yellow lines in Fig. 7), which resulted in the formation of sea fog near the surface (lower panel in Figs. 4a and 4c). As the fog deepened, LRC intensified at the surface fog layer (blue line in Fig. 7a). The sea fog formed from the surface is also shown in Figure 8, which depicts the vertical profiles of the hourly accumulated tendencies of temperature, Qv, and Qc in region A before the onset (1100 UTC) and at the onset (1200 UTC) of the sea fog on 15 April 2012. Cooling within the MABL in conjunction with LRC compensates for warm advection with the southerly wind at 1100 UTC on 15 April 2012, and the resulting heat budget led to cooling near the surface (black lines below z = 50 m in Figs. 8a, 8b, and 8c). At this time, moistening by advection existed below a height of 100 m (green lines in Figure 8a, 8d, and 8g). It is understood that the thermal and moisture conditions were favorable for the formation of conventional advection fog from the surface (Figure 8b, 8e, and 8h).

Preprints (www.preprints.org) | NOT PEER-REVIEWED | Posted: 5 March 2021 doi:10.20944/preprints202103.0177.v1

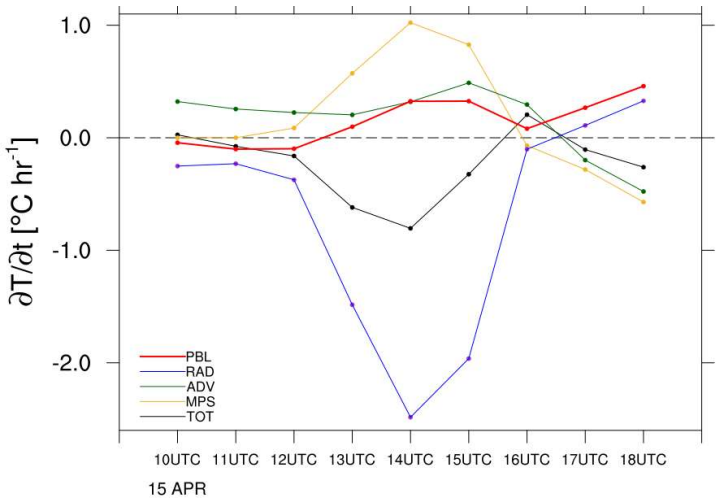

(a)

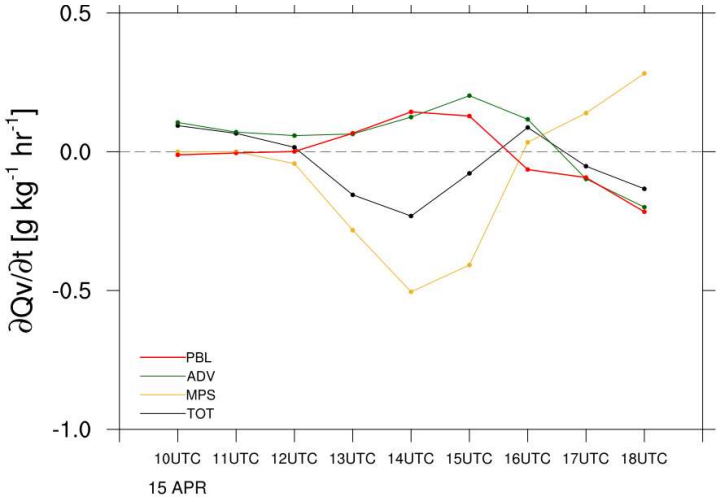

(b)

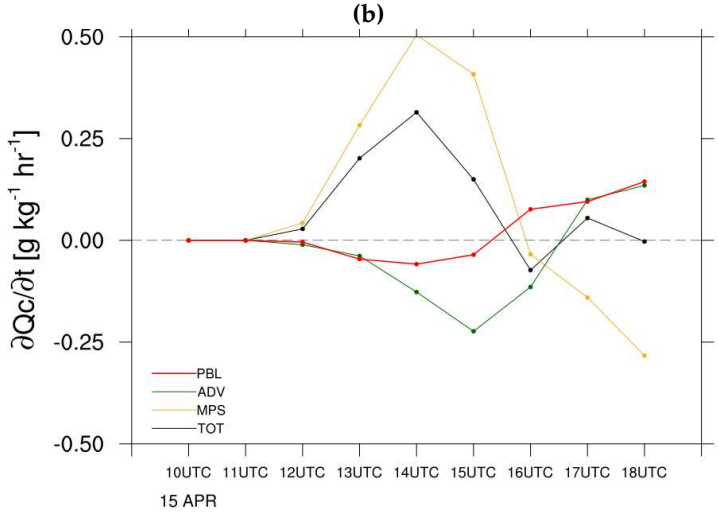

(c)

Figure 7. Time series of the hourly accumulated tendencies of the (a) temperature (°C hr^{-1}), (b) Qv (g kg^{-1} hr^{-1}), and (c) Qc (g kg^{-1} hr^{-1}) at z_1 in region A during the formation and evolution stages.

Preprints (www.preprints.org) | NOT PEER-REVIEWED | Posted: 5 March 2021 doi:10.20944/preprints202103.0177.v1

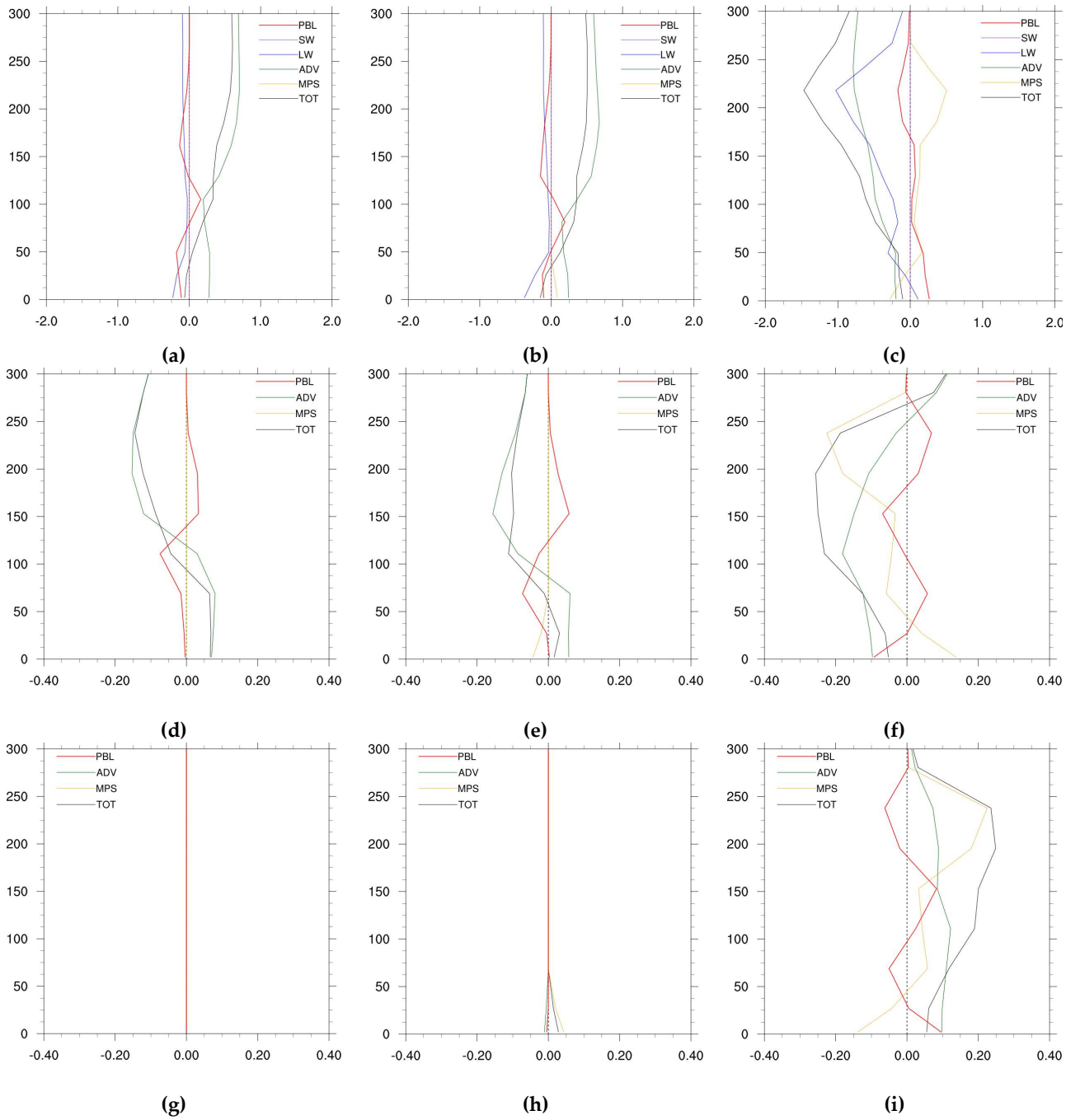

Figure 8. Vertical profiles of the hourly accumulated tendencies of (a–c) temperature (°C hr^{-1}), (d–f) Qv (g kg^{-1} hr^{-1}), and (g–i) Qc (g kg^{-1} hr^{-1}) in region A; (a, d, g) 1100 UTC (before the onset of the fog), (b, e, h) 1200 UTC (after the onset of the fog), and (c, f, i) 1700 UTC (at the vertical jump of the fog) on 15 April in 2012.

3.2.2. Evolution stage

A larger decrease in SAT led to a transformation of the SHF from negative to positive and an increase in latent heat flux (LHF) at 1400 UTC on 15 April 2012 (Figure 6a). SST and SAT observed from AWS and buoy data at Deokjeok island near Baeknyeong island were examined (Fig. 9), and can be used to infer the transition of turbulent fluxes. It indicates that SST was higher than the SAT observed during the evolution stage of the sea fog (1400 UTC 15 April 2012), unlike in the formation stage. This transition was consistent

Preprints (www.preprints.org) | NOT PEER-REVIEWED | Posted: 5 March 2021 doi:10.20944/preprints202103.0177.v1

with the simulated turbulent fluxes, as shown in Figure 6a, thus it is confirmed that the case belongs to the advection fog with ssH. The change in the surface turbulent flux enhanced vertical turbulent mixing within the MABL by a positive buoyant force. Enhanced turbulent mixing and moistening increased the depth of the sea fog and increased the MABL height, even at night (Figs. 4c and 6b). LRC was intensified at the top of the condensed layer after the onset of sea fog, and height with maximum LRC increased as the fog was formed (blue line in Fig. 7c), which contributed to the enhancement of the thermal instability. Local moistening at a lower atmosphere was possible due to the increase in the LHF (self-moistening) after this stage, and the supply of moisture originated from the moist advection before the onset of sea fog. It can be noted that the conditions of self-moistening and the ocean being warmer than the atmosphere changed to be favorable for the formation of warm advection fog with ssH, thus the mixed type of fog with ssH and fog with ssC was observed in this case. This is consistent with the case in which ssH usually occurs at the evolution stage of a sea fog event when the fog depth is typically greater than that at fog onset [3]. The temperature difference between the sea surface and surface air is generally robust during fog events in summer and winter seasons (e.g., summer: SAT > SST; winter: SST > SAT). However, the results of this study suggest that the difference of temperature is very small in spring and fall seasons, implying that the sign of surface turbulent fluxes can be easily changed. Thus, the new classification for a mixed type of fog with both ssC and ssH is needed.

The rapid vertical jump in the increase in the fog height is shown in the evolution of the vertical profile of the Qc in region A around 1600–1800 UTC on 15 April 2012 (Fig. 4c). In this case, the synoptic-scale condition changed the wind direction from southerly to northerly at about 1600 UTC on 15 April 2012. Accordingly, cold advection was induced by the northerly wind, and its maximum occurred at about z = 220 m (green line in Fig. 8c). This intensified atmospheric cooling in all of the layers below 300 m (Fig. 8c), which caused the formation of the fog on the layer by the microphysics process (Fig. 8i). This also led to an increase in the height with the maximum of LRC (blue line in Fig. 8c). This cooling at higher levels and the increase in surface positive turbulent fluxes (red lines in Fig. 6a and Fig. 8c) increased the thermal instability within the MABL, resulting in rapid upward diffusion of the fog and increased MABL height (Fig. 6b).

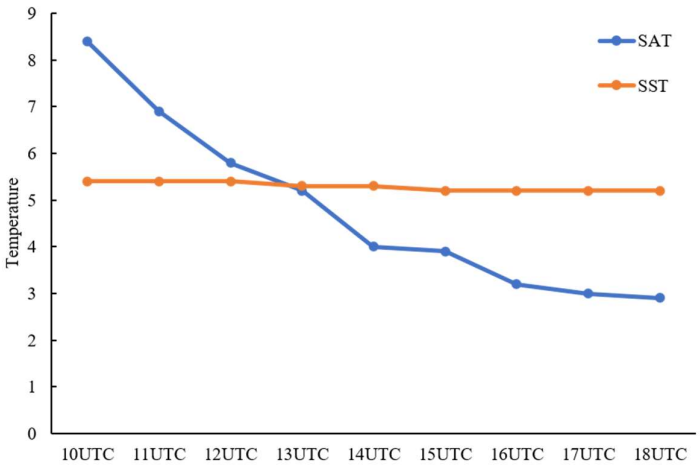

Figure 9. Sea surface temperature (SST) and surface air temperature (SAT) observed from AWS and buoy data at Deokjeok island.

Preprints (www.preprints.org) | NOT PEER-REVIEWED | Posted: 5 March 2021 doi:10.20944/preprints202103.0177.v1

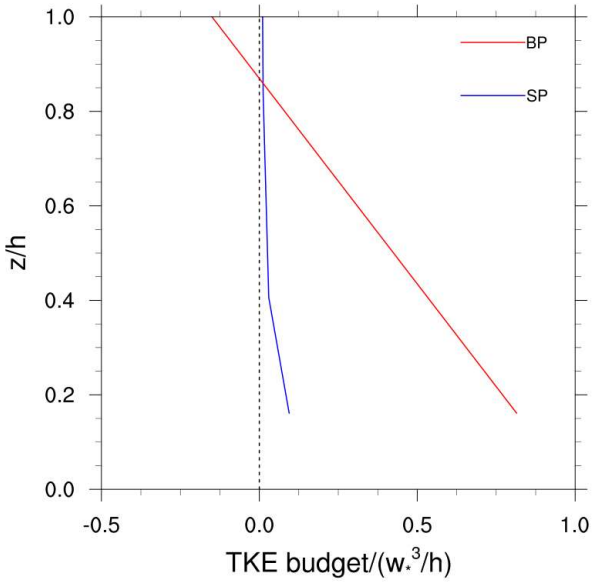

Figure 10. Turbulent kinetic energy (TKE) budget from the simulation, normalized by surface buoyancy production: buoyancy production (BP, red line) and shear production (SP, blue line).

To examine the nature of turbulence in the MABL, each budget term of turbulent kinetic energy (TKE) (mechanical production, buoyant production/loss, and turbulent transport of TKE and dissipation) normalized by surface buoyancy production $g/\overline{\theta_v}\left(\overline{w'\theta_v'}\right)_s$ was compared using the method suggested by previous studies [29–30].

They suggested that buoyant production/loss and mechanical production are a function of $z_*(=-z/L)$, as follows:

$$\mathrm{BP} = \begin{cases} 1 - 1.15z_*, & 0 < z_* \le 0.87 \\ -13.81 + 49.96z_* - 58.78{z_*}^2 + 22.53{z_*}^3, & 0.87 \le z_* \le 1 \end{cases} \quad (1)$$

$$\mathrm{SP} = -\frac{L}{h}\frac{[1 - 15(h/L)z_*]^{-1/4}}{z_*} \quad (2)$$

where L is the Monin–Obukhov length scale, and h is the MABL height. They reported that the method assumes that the change of momentum flux with height occurs within a small range. Thus, the method is used to evaluate TKE from the planetary boundary layer (PBL) scheme when mechanical production contributes less to the TKE budget than the buoyant production/loss does above the surface layer, for $-h/L > 10$. In this study, $-h/L$ had a large positive value of 23.75, indicating the stability of the MABL in the fog layer was unstable at the evolution stage. It supports the fact that the turbulence in the fog with ssH had the characteristics of a convective boundary layer (i.e., $-h/L > 10$) even at night [31]. Before the rapid growth of the fog, however, it was a negative value of −4.45, implying that the MABL was stable during the formation stage. This indicates that the turbulence had a different impact on the growth of the MABL in accordance with the fog with ssC and fog with ssH, and the MABL structure for the fog with ssH was systematically distinct from that for ssC [3]. Figure 10 shows each TKE budget by mechanical production and buoyant production/loss at 1630 UTC on 15 April 2012 from the simulation. During a strongly upward diffusion, the TKE budget implies that the buoyant production made a larger contribution to the TKE production than the wind shear, and the buoyant forcing originated from cooling above the top of the MABL due to cold advection and LRC at the top of fog layer, and warming due to an increase in the surface turbulent fluxes. This implies that the enhanced turbulent mixing in the interior of the fog layers was caused by thermal forcing, while the turbulence produced by mechanical forcing was small enough to be negligible in the MABL. It can be noted that cold advection can induce a rapid

Preprints (www.preprints.org) | NOT PEER-REVIEWED | Posted: 5 March 2021 doi:10.20944/preprints202103.0177.v1

increase in the MABL by enhancing the thermal instability. In addition, heat and moisture supplied from the ocean surface are confined in the MABL due to the strong subsidence inversion formed in the downward branch of a subtropical high in warm-sea fog phases, frequently resulting in the formation of low-level clouds or sea fogs [31].

The enhanced turbulent mixing contributed to warming/drying within the MABL and cooling/moistening above the MABL. Strong dry advection due to the transition of the wind direction was also dominant within the MABL at 1700 UTC on 15 April 2012 (Figs. 7b and 8f), which resulted in a decrease in RH. This contributed to the dissipation of the fog by evaporation. However, fogs formed in other regions also moved to this region (Figs. 7c and 8i). Consequently, the total amount of fog can be maintained by the balance between an increase in evaporation from a lower level of the MABL due to a decrease in RH and fog advection occurring in other regions.

3.2.3. Dissipation stage

Figure 11 shows the vertical profiles of the hourly accumulated tendencies at 0000 UTC and 0300 UTC on 16 April in 2012, when the fog began to dissipate above the MABL. After sunrise, the condensed layer absorbed SW, which offsets the LRC. At this time, cold advection was identified in the lower part of the MABL, whereas warm advection was found near the top of the MABL, due to the change in a large-scale flow. In addition, a large increase in positive SHF can be induced by warming near the surface. In this situation, the thermal instability and positive buoyant flux within the MABL were gradually weakened, which resulted in a gradual decrease in MABL height, even during the day. Meanwhile, enhanced surface turbulent fluxes led to warming and drying within the MABL, and dry advection was induced by the northerly wind. Thus, evaporation was enhanced in the lower MABL, despite an increase in LHF, showing an increase in Qv and a decrease in Qc in the microphysics processes, which contributed to dissipation of the fog. In addition, the amount of Qc near the top of the MABL was larger than that near its bottom. Turbulent mixing redistributed the fog from the top of the MABL into the lower MABL, thus, the density of the fog tended to decrease. Although advection of Qc that is formed in other regions also contributes to the amount of Qc, it appears to be minor or to have the opposite effect at the end of duration of the fog event because the dissipation was also observed in other regions (not shown).

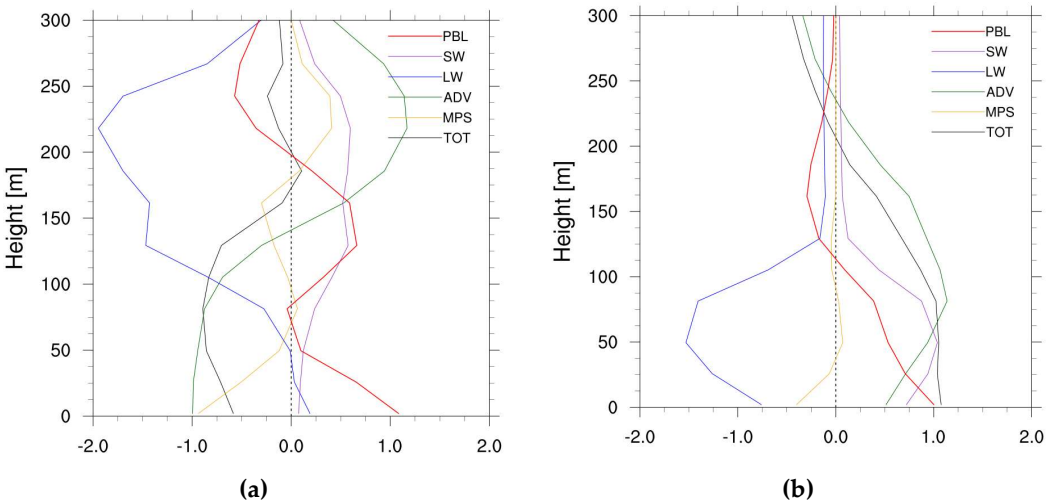

Preprints (www.preprints.org) | NOT PEER-REVIEWED | Posted: 5 March 2021 doi:10.20944/preprints202103.0177.v1

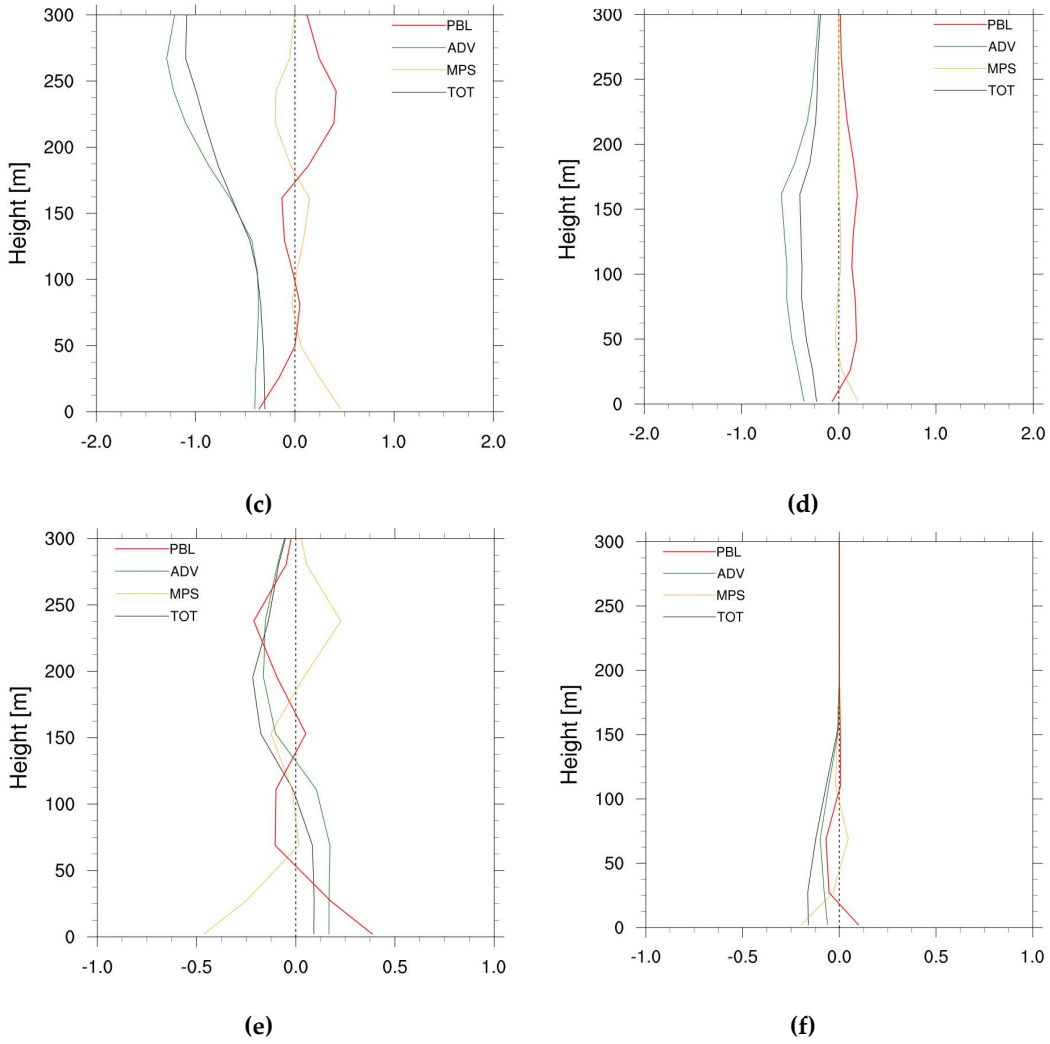

Figure 11. Vertical profiles of the hourly accumulated tendencies of (a, b) temperature (°C hr^{-1}), (c, d) Qv (g kg^{-1} hr^{-1}), and (e, f) Qc (g kg^{-1} hr^{-1}) in region A: (a) 0000 UTC (before the dissipation of the fog), and (b) 0300 UTC (after the dissipation of the fog) on 16 April in 2012.

3.2.4. Role of advection of Qc

The formation of the condensed layer in region B started at a certain height above the ground, thus, it is expected that the mechanism for the formation of sea fog in this region was different than that in region A. RH lower than 95% appeared in region B, thus, it was insufficient to be saturated at a height of about 200 m where the condensed layers appeared (Figs. 4b and 4d). To understand the causes of sea fog in region B, time series of the hourly accumulated tendencies of the Qc in this region during the period of fog (from 0400 UTC to 1200 UTC on 16 April) were investigated (Fig. 12). The mechanism can be explained using the average of the tendencies within a certain layer (300 m) because the condensed layers appeared to be centered on a height of about 200 m, unlike in region A. The sea fog can be placed in region B due to advection of Qc. This suggests that advection of Qc itself can control the local amount of sea fog without condensation in the microphysics process, in which RH is lower. Although the fog was distributed in region B, it was dissipated by evaporation in the microphysics process, due to lower RH.

Furthermore, enhanced turbulent mixing and the entrainment process during the day played a role in the vertical diffusion of the sea fog from the MABL to close to the surface because the density of Qc was higher at a certain height, and led to a downward

Preprints (www.preprints.org) | NOT PEER-REVIEWED | Posted: 5 March 2021 doi:10.20944/preprints202103.0177.v1

shift of the fog layer (Fig. 13). In addition, the shift accelerated as the MABL height decreased at night. Consequently, the bottom of the fog touched the surface.

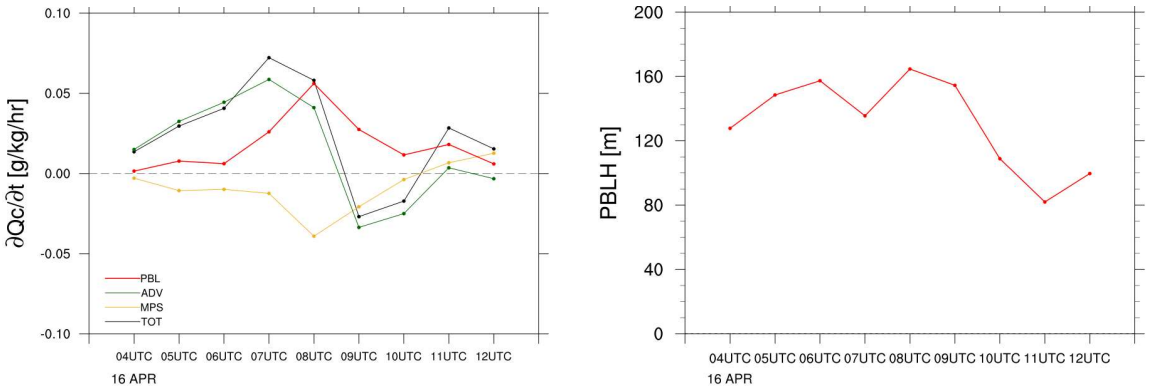

Figure 12. Time series of the (a) hourly accumulated tendency of Qc (g kg^{-1} hr^{-1}) averaged for levels below a height of 300 m and (b) MABL height in region B during the fog event.

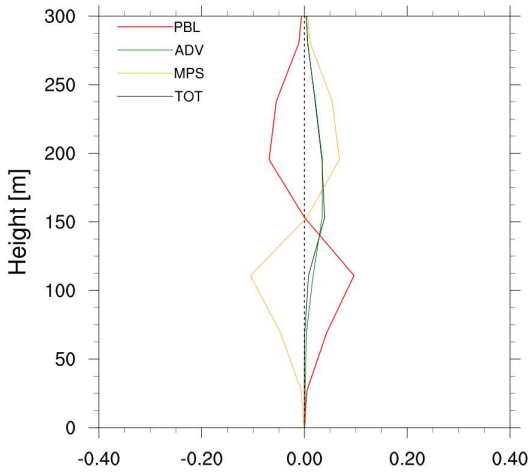

Figure 13. Vertical profiles of the hourly accumulated tendency of Qc (g kg^{-1} hr^{-1}) in region B at 0400 UTC on 16 April in 2012.

3.2.5. Sensitivity test to sea surface salinity

In most models of numerical weather prediction, the ocean surface is assumed to be saturated with pure water in the bulk formula for estimating surface turbulent fluxes, such as SHF and LHF. However, previous research has emphasized the importance of sea surface salinity in numerical weather forecasts. Studies have reported that the resulting dryness within the MABL due to the sea surface salinity improves the simulated convective precipitation [32]. Therefore, the impact of sea surface salinity on the evolution of the fog is discussed in this section.

According to Raoult's Law, the saturated vapor pressure with respect to seawater is lower than that with respect to pure water. It was suggested in a previous study that the saturated vapor pressure with respect to seawater in terms of the saturated vapor pressure with respect to pure water is expressed as [32]:

$$e_{s,sw} = \frac{e_{s,pw}}{1 + 0.57357[S/(1000 - S)]} \quad (3)$$

Preprints (www.preprints.org) | NOT PEER-REVIEWED | Posted: 5 March 2021 doi:10.20944/preprints202103.0177.v1

where $e_{s,sw}$ and $e_{s,pw}$ is the saturated vapor pressure for seawater and pure water (hPa), respectively, and S is the sea surface salinity (psu). To investigate the impact of sea surface salinity on the evolution of the sea fog, this revised saturated vapor pressure was used in an additional experiment. The initial condition for sea surface salinity was taken from salinity values of the Argo gridded dataset (http://apdrc.soest.hawaii.edu/projects/Argo/data/gridded/On_standard_levels/index-1.html), which was produced by International Pacific Research Center (IPRC). Most Argo data do not have a salinity value on the surface. Accordingly, the first-level depth (5 m) was used as the sea surface salinity because it could be assumed that the ocean mixed layer has homogenous salinity. Hereafter, the previous experiment is referred to as CTL and this experiment is referred to as SAL.

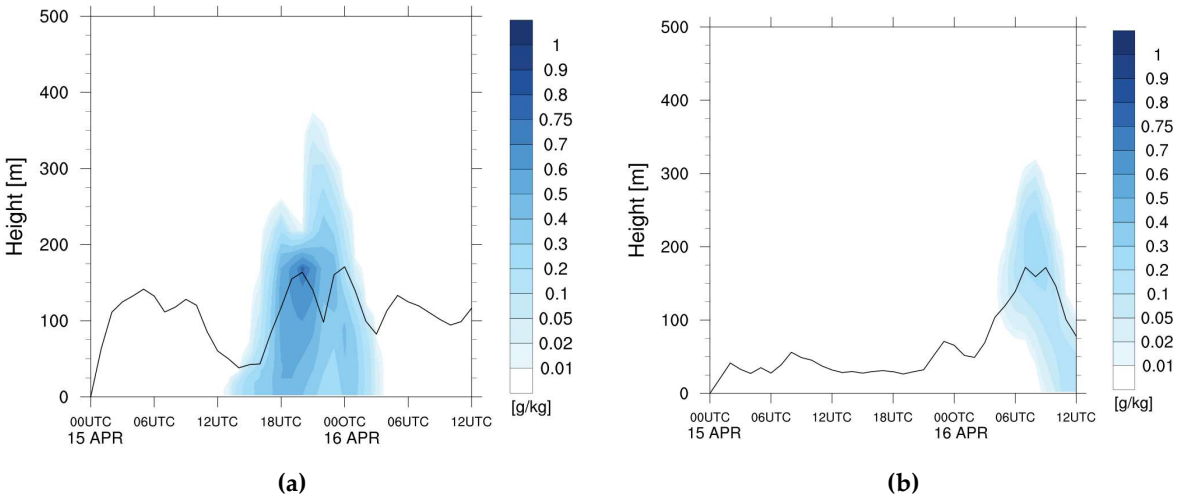

Figure 14. Evolution of vertical profiles of the Qc (g kg^{-1}) in (a) region A and (b) region B simulated from SAL.

It was found that incorporating the salinity effect in the numerical simulation decreases LHF due to the decrease in the saturated vapor pressure and specific humidity over the ocean surface. A decrease in LHF implies less transport of moisture from the ocean to the atmosphere during the fog event. Meanwhile, it was observed that the salinity effect had little influence on the SHF. Figure 14 represents the evolution of vertical profiles of the Qc simulated from SAL. SAL tends to simulate weaker and shallower fog, compared to CTL, due to a smaller amount of Qc during the fog event.

The rapid vertical jump of the fog also appears in SAL, similar to that in CTL. SAL simulated a synoptic-scale condition that was similar to that in CTL. Cold advection caused by the northerly wind due to the change in the large-scale flow was also shown, thus, an increase in thermal instability was also observed (not shown). According to the results, it was established that the rapid growth of sea fog was predominantly induced by cold advection.

The difference in sea fog between CTL and SAL is shown in the comparison of the top heights and amounts of the sea fog (Fig. 15). The top heights and amounts of the sea fog were estimated as the maximum height with Qc of 0.01 g kg^{-1} and Qc averaged for the levels lower than a height of 500 m. In SAL, the top height was lower, and the formation and dissipation also occurred 1 h later and earlier, respectively, compared to that in CTL. In addition to the top height of the fog, the smaller amount of Qc was also simulated in SAL, which can influence higher visibility. It was caused by a decrease in LHF and weakening self-moistening locally, which resulted in suppressing the condensation in the microphysics process under the drier condition. This suggests that considering sea surface

Preprints (www.preprints.org) | NOT PEER-REVIEWED | Posted: 5 March 2021 doi:10.20944/preprints202103.0177.v1

salinity in the short-term weather prediction model predominantly has an impact on the formation, evolution, and dissipation processes of the sea fog.

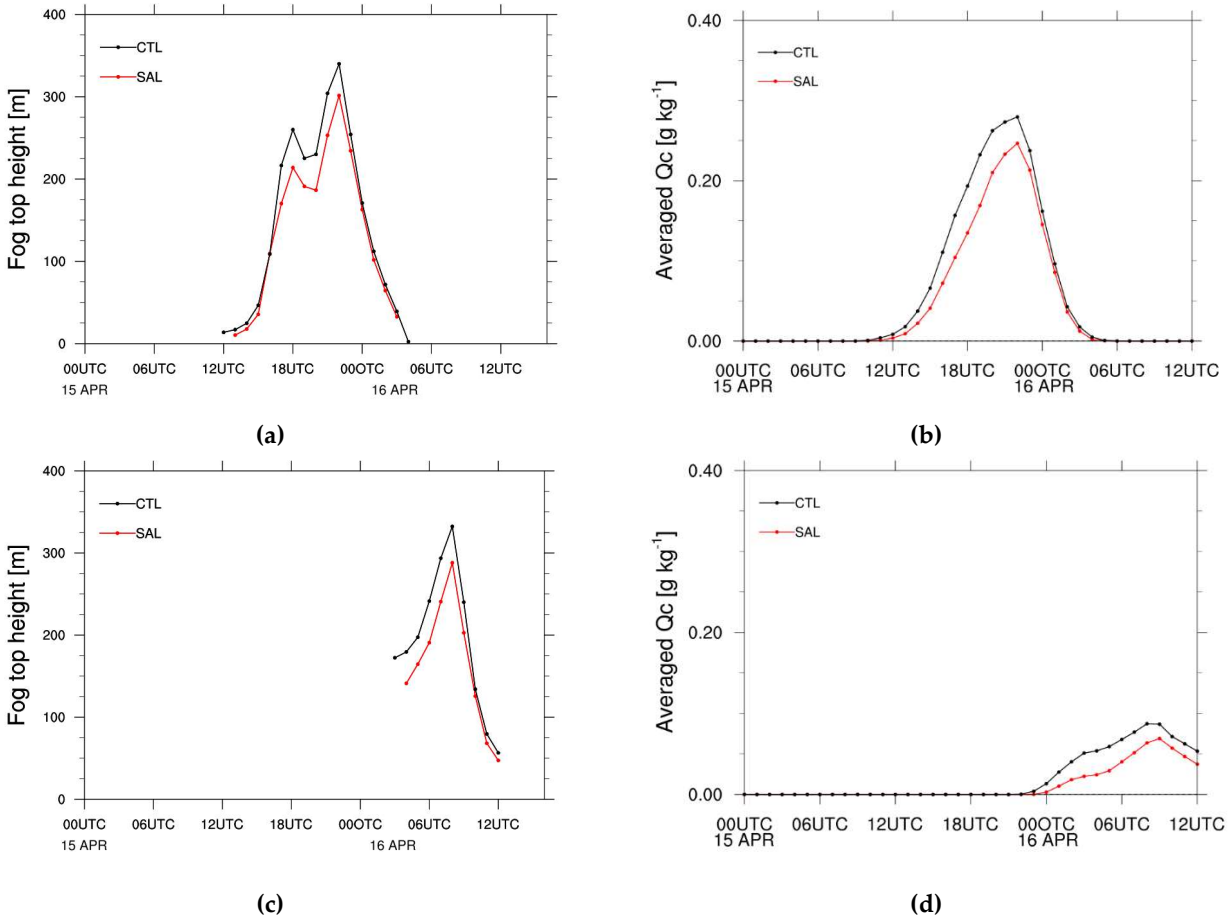

Figure 15. Time series of the estimated height of the (a, c) fog top (m) and (b, d) Qc averaged for the levels lower than a height of 500 m (g kg^{-1}) from CTL (black line) and SAL (red line): (a, b) region A and (c, d) region B.

4. Concluding remarks

To understand the mechanisms in the formation, evolution, and dissipation stages of sea fog, particularly warm advection fog with ssH, a sea fog event over the eastern Yellow Sea on 15–16 April 2012 was investigated using a high-resolution numerical simulation of the WRF model after it was verified by satellite data and in-situ data. The verification showed that the simulation had a good agreement with the observations in the formation, evolution, and dissipation phases of the sea fog. Initially, moist advection and cooling at z_1 by negative SHF and LRC triggered the formation of the sea fog near the surface, and this fog was a conventional type of advection fog. Then, intensified cooling near the surface transformed the SHF from negative to positive and increased LHF, which enhanced turbulent mixing. Increased LHF also moistened the lower atmosphere locally without moist advection, resulting in favorable conditions for fog with ssH. Enhanced turbulent mixing and moistening due to surface turbulent flux increased the depth of the sea fog and the MABL height, even at night. This suggests that turbulence has a different impact on the growth of the MABL in accordance with the fog with ssC and fog with ssH. In this case, cold advection due to the change to a northerly synoptic wind and the maximum LRC at the top of condensed layer led to strong upward diffusion of the fog. It was proven using TKE budget analysis that cold advection contributed to a rapid increase in the MABL resulting from strong positive buoyant forcing due to an increase in thermal

instability. After sunrise, SW warming offsetting the LRC reduced the MABL height, which resulted in trapping the fog within the low atmosphere. In addition, dry advection contributed to the dissipation of the fog due to the increase in evaporation. Furthermore, the advection of Qc plays an important role in controlling the local amount of fog, in which RH is not sufficient for saturation to cause fog. Finally, an additional sensitivity test considering sea surface salinity showed weaker and shallower sea fog than the control run due to a decrease in both latent heat flux and self-moistening locally. Thus, it can be expected that the overestimation of its depth was alleviated.

This case study improves our understanding of all processes related to the formation, evolution, and dissipation of sea fog, which can eventually help future studies for a detection of warm advection fog using remote sensing and/or in-situ observations. In particular, this study investigated the mechanism of advection fog with ssH and suggests that the turbulence is associated with all phases of the formation, growth, and dissipation of the sea fog, although numerous studies on the mechanism of sea fog have focused on the radiation and microphysics processes. However, further studies are still needed to verify the simulated fog. First, it is clear that a rapid upward diffusion is strongly related to turbulence, and can be highly dependent on the PBL scheme. Thus, overestimation of the height of the sea fog top should be confirmed by investigating the sensitivity of its vertical diffusion in various PBL schemes (e.g., local schemes vs. nonlocal schemes). Second, although the existence and visibility of sea fog can be validated using satellite and in situ observed data, the vertical structure can be also validated using information estimated from satellite sensors. However, this approach has limitations: information from satellites is not available under cloudy conditions (e.g., satellites with infrared sensors), and polar orbiting satellites do not provide continuous information for the diurnal evolution of the sea fog. Thus, it is difficult to confirm the overestimation of sea fog in the simulation. Therefore, intense observational sites (i.e., super sites) and/or field campaigns focusing on various fog events under different synoptic-scale conditions are needed to understand more detailed generation mechanisms of fog evolution by measuring the height of the fog top and turbulent fluxes directly. This will provide more useful information for improving fog forecasts, helping to reduce possible accidents and damage in transportation operations under low visibility conditions due to the fog.

Author Contributions: Eunjeong Lee (EL) and Jung-Hoon Kim (JHK) performed the analysis and wrote the main body of the manuscript. EL ran the model, and takes responsibility for data curation and quality control. JHK conceptualized the idea of the project, and supervised the computer and funding resources. Ki-Young Heo (KYH) provided scientific advice to support the project. Yang-Ki Cho (YKC) took a responsibility for the project administration, provided invaluable scientific suggestions and comments. EL wrote the original manuscript, and JHK reviewed and edited the original manuscript. All authors contributed critical feedback to this paper.

Funding: This work was funded by the Korea Meteorological Administration Research and Development Program under Grant KMI2020-01910, and was also supported by the Basic Science Research Program through the National Research Foundation of Korea (NRF) funded by the Ministry of Education (NRF-2019R1I1A2A01060035).

Acknowledgments: We thank two anonymous reviewers and editors for their invaluable comments and suggestions on the original manuscript. We thank Dr. Kook-Jin Kim at the Underwater Survey Technology 21 (UST21) company and Dr. Young-Taek Kim at the Korea Hydrographic and Oceanographic Agency (KHOA) for their supports for the project. This work was also supported by project of 'Machine Learning-Based Prediction and Accuracy Improvement of Sea Fog Dissipation' funded by the KHOA.

References

1. Garmon, J.F.; Darbe D.L.; Croft P.J. Forecasting significant fog on the Alabama coast: Impact climatology and forecast checklist development. *NWS Technical Memorandum NWS SR* **1996**, *176*, pp. 16.
2. Koračin, D.; Dorman, C.E.; Lewis, J.M.; Hudson, J.G.; Wilcox, E.M.; Torregrosa, A. Marine fog: A review. *Atmos. Res.* **2014**, *143*, 142–175, 10.1016/j.atmosres.2013.12.012.
3. Yang, L.; Liu, J.-W.; Ren, Z.-P.; Xie, S.-P.; Zhang, S.-P.; Gao, S.-H. Atmospheric conditions for advection-radiation fog over the western Yellow Sea. *J. Geophys. Res.:Atmos.* **2018**, *123*, 5455–5468. 10.1029/2017JD028088.
4. Kim, C.-K.; Yum, S.-S. Local meteorological and synoptic characteristics of fogs formed over Incheon international airport in the west coast of Korea. *Adv. Atmos. Sci.* **2010**, *27(4)*, 761–776, 10.1007/s00376-009-9090-7.
5. Cho, Y.-K.; Kim, M.-O.; Kim, B.-C. Sea fog around the Korean Peninsula. *J. Appl. Meteorol.* **2000**, *39(12)*, 2473–2479. 10.1175/1520-0450(2000)039%3C2473:SFATKP%3E2.0.CO;2.
6. Zhang, S.-P.; Xie, S.-P.; Liu, Q.-Y.; Yang, Y.-Q.; Wang, X.-G.; Ren, Z.-P. Seasonal variations of Yellow Sea fog: Observations and mechanisms. *J. Clim*. **2009**, *22(24)*, 6758–6772, 10.1175/2009JCLI2806.1.
7. Gultepe, I.; Isaac, G.; Williams, A.; Marcotte, D.; Strawbridge, K. Turbulent heat fluxes over leads and polynyas and their effect on Arctic clouds during FIRE-ACE: Aircraft observations for April 1998. Atmosphere and Ocean, **2003**, *41(1)*, 15-34.
8. Croft, P.J.; Darbe D.L.; Garmon J.F. Forecasting significant fog in southern Alabama. *Natl. Weather Dig.* **1995**, *19*, 10–16.
9. Gultepe, I.; Pagowski, M.; Reid, J. A Satellite-Based Fog Detection Scheme Using Screen Air Temperature. *Wea. Forecast.*, **2007**, *22*, 444-456.
10. Gultepe, I.; Muller, M.D.; Boybeyi, Z. A New Visibility Parameterization for Warm-Fog Applications in Numerical Weather Prediction Models. *J. Appl. Meteorol. Climatol.* **2006**, *45*, 1469-1480.
11. Gultepe I.; Isaac, G.A. Effects of air mass origin on Arctic cloud microphysical parameters for April 1998 during FIRE.ACE. J. Geophys. Res. 2002, 107(C10), SHE-4-1-SHE4-12.
12. Kim, C.-K.; Yum, S.-S. A numerical study of sea-fog formation over cold sea surface using a one-dimensional turbulence model coupled with the Weather Research and Forecasting Model. *Boundary Layer Meteorol.* **2012**, *143(3)*, 481–505, 10.1007/s10546-012-9706-9.
13. Skamarock, W.C.; Klemp, J.B.; Dudhia, J.; Gill, D.O.; Liu, Z.; Berner, J.; Wang, W.; Powers, J.G.; Duda, M.G.; Barker, D.M.; Huang, X.-Y. A description of the advanced research WRF version 4. NCAR Tech. note NCAR/TN556+STR, **2019**, pp.145.
14. Hong, S.-Y.; Noh, Y.; Dudhia, J. A new vertical diffusion package with an explicit treatment of entrainment processes. *Mon. Wea. Rev.* **2006**, *134(9)*, 2318–2341, 10.1175/MWR3199.1.
15. Lim, K.-S. S.; Hong, S.-Y. Development of an effective doublemoment cloud microphysics scheme with prognostic cloud condensation nuclei (CCN) for weather and climate models. *Mon. Wea. Rev.* **2010**, *138*, 1587-1612, 10.1175/2009MWR2968.1.
16. Mlawer, E.J.; Taubman, S.J.; Brown, P.D.; Iacono, M.J.; Clough, S.A. Radiative transfer for inhomogeneous atmospheres: RRTM, a validated correlated-k model for the longwave. *J. Geophys. Res.* **1997**, *102(D14)*, 16,663–16,682, 10.1029/97JD00237.
17. Chen, F.; Dudhia, J. Coupling an advanced land surface hydrology model with the Penn State–NCAR MM5 modeling system. Part I: Model implementation and sensitivity. *Mon. Wea. Rev.* **2001**, *129*, 569–585, 10.1175/1520-0493(2001)129,0569:CAALSH.2.0.CO;2.
18. Ek, M.B.; Mitchell, K.E.; Lin, Y.; Rogers, E.; Grunmann, P.; Koren, V.; Gayno, G.; Tarpley, J.D. Implementation of Noah land surface model advances in the National Centers for Environmental Prediction operational mesoscale Eta model. *J. Geophys. Res.* **2003**, *108*, 8851, 10.1029/2002JD003296.
19. Tewari, M.; Chen, F.; Wang, W.; Dudhia, J.; LeMone, M.A.; Mitchell, K.; Ek, M.; Gayno, G.; Wegiel, J.; Cuenca, R.H. Implementation and verification of the unified NOAH land surface model in the WRF model. 20th conference on weather analysis and forecasting/16th conference on numerical weather prediction, **2004**, pp. 11–15.
20. Jiménez, P. A.; Dudhia, J.; Gonzále-Rouco J. F.; Navarro, J.; Montávez, J. P.; García-Bustamante, E. A revised scheme for the WRF surface layer formulation. *Mon. Wea. Rev.* **2012**, *140(3)*, 898–918, 10.1175/MWR-D-11-00056.1.
21. Kain, J.S.; Fritsch, J.M. Convective parameterization for mesoscale models: the Kain-Fritsch scheme. *The representation of cumulus convection in numerical models*, Emanuel, K. A., and Raymond, D. J., Eds., Amer. Meteor. Soc., **1993**, pp. 165-170.
22. Ellrod G.P. Advances in the detection and analysis of fog at night using GOES multispectral infrared imagery. *Wea. Forecast*. **1995**, *10(3)*, 606–619.
23. Underwood S.J.; Ellrod G.P.; Kuhnert A.L. A multiple-case analysis of nocturnal radiation-fog development in the central valley of California utilizing the GOES nighttime fog product. *J. Appl. Meteorol*. **2004**, *43(2)*, 297–311.
24. Yamanouchi T.; Suzuki K.; Kawaguchi S. Detection of clouds in Antarctica from infrared multispectral data of AVHRR. *J. Meteorol. Soc. Jpn*. **1987**, *65*, 949–962.

25. Steeneveld, G. J.; Tolk, L. F.; Moene, A. F.; Hartogensis, O. K.; Peters, W.; Holtslag, A. A. M. Confronting the WRF and RAMS mesoscale models with innovative observations in the Netherlands: Evaluating the boundary layer heat budget, *J. Geophys. Res.*, **2011**, 116, D23114, doi:10.1029/2011JD016303.
26. Lin, C.; Zhang, Z.; Pu, Z. Numerical simulations of an advection fog event over Shanghai Pudong International Airport with the WRF model. *J Meteorol Res.* **2017**, *31*, 874–889. 10.1007/s13351-017-6187-2.
27. Carlos R.-C.; Carlos Y.; Gert-Jan S.;, Gema M.; Jon A. A.; Mariano S.; Gregorio M. Radiation and cloud-base lowering fog events: Observational analysis and evaluation of WRF and HARMONIE, *Atmos. Res.* **2019**, *229*, 190-207, 10.1016/j.atmosres.2019.06.018.
28. Lee, H.-Y.; Chang, E.-C. Impact of land-sea thermal contrast on the inland penetration of sea fog over the coastal area around the Korean Peninsula. *J. Geophys. Res.:Atmos.* **2018**, *123*, 6487–6504.
29. Lenschow, D. H.; Model of the height variation of the turbulent kinetic energy budget in the unstable planetary boundary layer. *e***1974**, *31*, 465–474.
30. Shin, H. H.; Hong, S.-Y.; Noh, Y.; Dudhia, J. Derivation of Turbulent Kinetic Energy from a First-Order Nonlocal Planetary Boundary Layer Parameterization. *J. Atmos. Sci.* **2013**, *70 (6)*, 1795–1805. 10.1175/JAS-D-12-0150.1.
31. Kim, C.-K.; Yum, S.-S. Marine Boundary Layer Structure for the Sea Fog Formation off the West Coast of the Korean Peninsula. *Pure Appl. Geophys.* **2012**, *169*, 1121–1135.
32. Lee, E.; Hong, S.-Y. Impact of the sea surface salinity on simulated precipitation in a global numerical weather prediction model. *J. Geophys. Res.:Atmos.* **2019**, *e*, 719–730, 10.1029/2018JD029591.